ELSEVIER

### Contents lists available at ScienceDirect

# Acta Materialia

journal homepage: www.elsevier.com/locate/actamat



# Ultrahigh tribocorrosion resistance of metals enabled by nano-layering



Wenbo Wang<sup>a</sup>, Kaiwen Wang<sup>a</sup>, Zhengyu Zhang<sup>a</sup>, Jia Chen<sup>a</sup>, Tianyou Mou<sup>b</sup>, F. Marc Michel<sup>c</sup>, Hongliang Xin<sup>b</sup>, Wenjun Cai<sup>a,\*</sup>

- <sup>a</sup> Department of Materials Science and Engineering, Virginia Polytechnic Institute and State University, Virginia 24061, United States
- <sup>b</sup> Department of Chemical Engineering, Virginia Polytechnic Institute and State University, Virginia 24061, United States
- <sup>c</sup> Department of Geosciences, Virginia Polytechnic Institute and State University, Virginia 24061, United States

# ARTICLE INFO

### Article history: Received 14 July 2020 Revised 15 December 2020 Accepted 25 December 2020 Available online 4 January 2021

Keywords:
Nanostructured multilayers
Tribocorrosion
Transmission electron microscopy
Finite element analysis
Density functional theory

### ABSTRACT

Tribocorrosion damage on metal surfaces imposes a great challenge to their reliable long-term performance in corrosive environment. In the present work, we showed that nanostructured metallic multilayers (NMMs) exhibited ultrahigh tribocorrosion resistance owing to abundant interfaces and nanoscale chemical modulation that effectively restricted plastic deformation, reduced micro-galvanic corrosion and surface reactivity. Specifically, the tribocorrosion behaviors of equal-spaced Al/X (X = Ti, Mg and Cu) NMMs with ~ 3 nm individual layer thickness were studied in 0.6 M NaCl aqueous solution under room temperature. Nanomechanical and electrochemical measurements were coupled with advanced material characterization tools to study the effects of constituting materials on the deformation and degradation mechanisms. It was found that while corrosion dominated in Al/Mg and Al/Cu NMMs, severe plastic deformation dominated in Al/Ti during tribocorrosion due to sustained surface passivity. A finite element (FE) based computational model was developed and validated to quantify the tribocorrosion behavior of all NMMs, which showed accelerated material loss at layer interfaces as well as wear track edge resulting from the synergistic effects of wear and corrosion. Finally, density functional theory (DFT) calculations were carried out to uncover the origin of corrosion resistance in NMM. It was found that via nanolayering, the surface work function of Al was increased while Cl adatoms adsorb less strongly than that on pure Al, thus reducing the surface reactivity and pitting susceptibility. The combined experimental and computational study provides a guideline for future material selection and design of multilayered and multi-phase metals for use under extreme environment.

© 2021 Acta Materialia Inc. Published by Elsevier Ltd. All rights reserved.

# 1. Introduction

The design of new metals and alloys resistant to both wear damage and corrosion degradation becomes increasingly demanded in complex service conditions, such as biomedical implants, hydraulic systems, nuclear power plants, marine and offshore infrastructures, etc. [1–7]. Recently, nanostructured metallic multilayers (NMMs) consisting of alternating layers of different metals or alloys have attracted significant interests due to their potential to simultaneously achieve improved mechanical and electrochemical properties compared to their monolithic counterparts [8,9]. Hence it is critical to understand how the structure and properties of the constituting materials and interfaces of NMMs can be tailored to simultaneously optimize their wear and corrosion resistance, i.e. tribocorrosion resistance. Previous research shows that the individual layer thickness (h) of NMMs governs their mechani-

cal and tribological behavior [10–12]. The wear rate of NMMs typically increases with decreasing hardness per Archard's law [13–15], although an optimum individual layer thickness of NMM for the highest wear resistance is not known *a priori* [16,17]. In addition to layer thickness effect, the elastic/plastic incompatibility between the constituting materials [18], the structure and properties of the heterophase interfaces [14,19], as well as residual stress [16,20] also play important roles on the tribological response of NMMs.

Apart from their excellent mechanical and tribological properties, many NMMs exhibit improved corrosion resistance compared to their monolithic counterpart of equal thickness due to the formation of less susceptible microstructure (e.g. finer grains and smoother surfaces) and the ability to effectively block ionic diffusion due to the presence of interfaces [8,9,21,22]. However, such low corrosion rate is often short-lived. As soon as localized corrosion penetrates through the top layer, the ensuring galvanic coupling between adjacent layers often leads to preferred corrosion of the more active layers thus destructing the overall structural

<sup>\*</sup> Corresponding author. E-mail address: caiw@vt.edu (W. Cai).

integrity. For example, in Zn/Ni NMMs, only Ni layers could be found after extended corrosion testing in 5 wt.% sodium chloride solution while all Zn sublayers were dissolved [22]. Hence optimizing corrosion resistance of NMMs requires an effective strategy that minimizes the micro-galvanic coupling between the constituting layers [23].

Even though there is no unified theory at the moment, the abundant evidence above indicates exciting opportunities to optimize tribocorrosion resistance of metals by forming nanostructured multilayers. For NMMs, the individual layer thickness not only controls its mechanical response due to length-scale dependent dislocation-mediated plasticity, but also represents the wavelength of chemical modulation, hence governs its electrochemical kinetics. Recent studies show that materials' corrosion resistance could be enhanced by controlling the chemical modulation below a critical length scale on the order of a few nm. For example, Ralston et al. [24] showed that when the precipitate size is below ~ 4 nm in Al-Cu-Mg alloys, the precipitates become 'invisible' during corrosion, i.e., they harden the material without forming unfavorable micro-galvanic coupling with the matrix. It was suggested that a continuous protective passive film could not be formed if the chemical heterogeneity length scale exceeds this threshold. Based on these separate observations on mechanical and corrosion properties, NMMs with individual layer thickness of a few nm, can potentially allow for achieving extensive ultra-fine chemical modulation across adjacent layers and hence represent a new class of material system for exploring fundamental chemistry and physics at the scale of a few atoms. However, the underlying deformation and degradation mechanisms of NMMs, and how the synergistic effects of the mechanical and electrochemical properties of the individual layers govern the overall tribocorrosion behavior, remains largely unknown.

This work aims to develop a fundamental understanding of equal-spaced Al/X (X=Mg, Ti, and Cu) NMMs, their structure, and their deformation and degradation mechanisms during tribocorrosion. Aluminum (Al) is chosen as the top layer for its high corrosion resistance and passivity in 0.6 M NaCl aqueous solution, while

Mg, Ti, and Cu were chosen to represent increasing thermodynamic driving force for corrosion, with more negative (-2.37 V vs. SHE), comparable (-1.63 V vs. SHE) and more positive (+0.34 V vs. SHE) standard electromotive force potential than that of Al (-1.66 V vs. SHE) [25]. Notably, the galvanic series of the four metals in seawater follows a slightly different trend: ranking from Mg, Al, Cu, to Ti with increasing corrosion potential (i.e. from active to noble) [26]. An individual layer thickness of ~ 3 nm was chosen for all samples. Specifically, nanoindentation and nanowear, potentiodynamic polarization, and tribocorrosion tests were performed to evaluate the effects of constituting materials on the tribological, corrosion, and tribocorrosion properties of Al/X NMMs. The microstructure of NMMs before and after tribocorrosion were characterized using scanning and transmission electron microscopies. Finally, finite element simulations and density functional theory calculations were performed to offer more insight on the localized corrosion and tribocorrosion mechanisms of NMMs.

#### 2. Experimental methods

### 2.1. Materials synthesis and characterization

Equal-spaced Al/X (X= Mg, Ti, and Cu) NMMs samples with alternating layers of Al and X were deposited on (100) Si substrate using direct current (DC) magnetron sputtering under a working pressure of 5 mTorr Argon atmosphere (PVD PRODUCTS, Wilmington, MA). The sputtering targets of 99.99% Al, 99.995% Ti, 99.99% Mg and 99.99% Cu were cleaned ~ 8 min at power of 200 W, 250 W, 50 W and 50 W respectively prior to sputtering to remove native oxides and surface contaminants. The substrate was subjected to a bias etch of ~ 5 min and then placed ~ 180 mm below the targets and rotated at 40 rpm during sputtering. All deposition started with metal X on Si substrate, followed by Al, as shown in Fig. 1(a). The individual thickness is ~ 3 nm and the total film thickness is ~ 1.74  $\pm$  0.1  $\mu$ m (Table 1). Additional monolithic thin films of Al, Ti, Mg and Cu (~ 1  $\mu$ m total thickness) were also prepared for comparison, as summarized in Table 2.

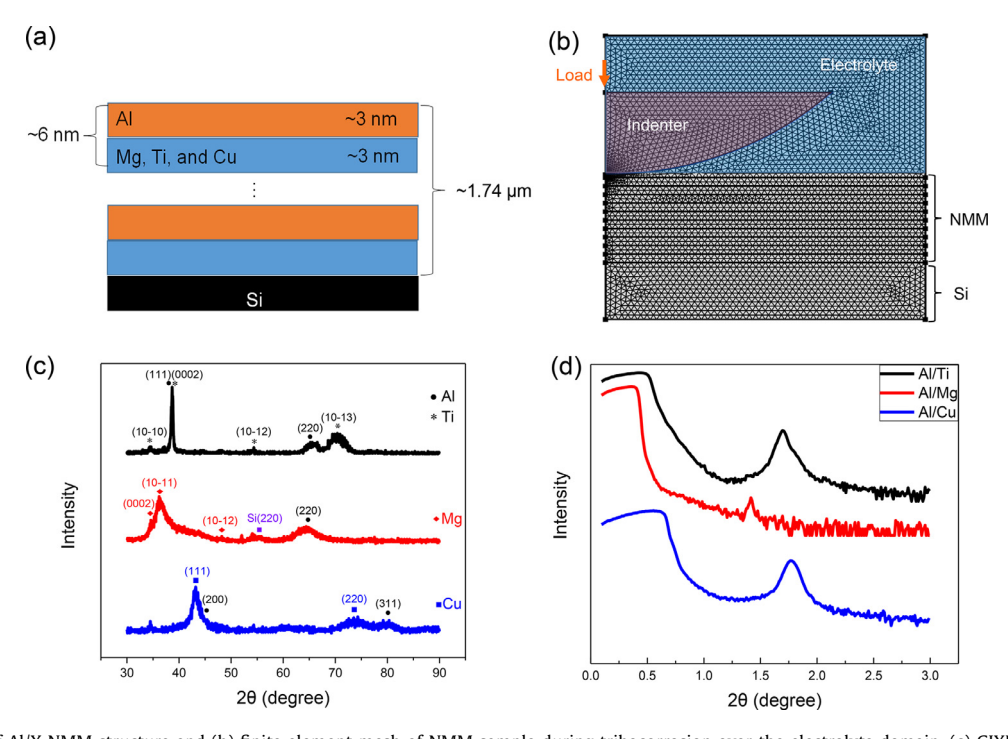


Fig. 1. (a) Schematic of Al/X NMM structure and (b) finite element mesh of NMM sample during tribocorrosion over the electrolyte domain. (c) GIXRD and (d) XRR patterns of Al/Ti, Al/Mg and Al/Cu multilayers.

**Table 1** Summary of bi-layer thickness and mechanical properties of all Al/X NMM samples.

NMM sample	Bi-layer thickness		Mechanical properties			
	XRR (nm)	TEM (nm)	H (GPa)	E (GPa)	H <sub>ROM</sub> (GPa)	
Al/Ti	$5.92\pm0.08$	$5.64\pm0.32$	$5.44\pm0.52$	$91.37 \pm 6.62$	1.61	
Al/Mg	$6.48\pm0.04$	NA	$3.81\pm0.26$	$59.98 \pm 2.21$	0.74	
Al/Cu	$5.71\pm0.11$	$5.48\pm0.43$	$6.3\pm0.54$	$97.64\pm6.05$	1.43	

**Table 2**Summary of key mechanical and corrosion properties of monolithic samples.

	Mechanical properties		Electrochemical properties		
sample	H (GPa)	E (GPa)	E <sub>corr</sub> (V vs. Ag/AgCl)	i <sub>corr</sub> (μA/cm <sup>2</sup> )	
Al		77.62 ± 14.2		$0.83\pm0.15$	
Ti	$2.55 \pm 0.46$	$68.35 \pm 4.01$	$-0.28 \pm 0.01$	$0.42 \pm 0.16$	
Mg	$0.8\pm0.14$	$34.28 \pm 1.98$	$-1.78 \pm 0.05$	$42.24 \pm 46.05$	
Cu	$2.18\pm0.07$	$58.23\pm4.36$	$-0.21\pm0.01$	$1.2\pm0.54$	

Grazing incidence X-ray diffraction (GI-XRD) and X-ray reflectometry (XRR) were conducted using PANalytical X'Pert PRO diffractometer with Cu K $\alpha$  radiation (1.5406 Å) at 45 kV and 40 mA. The incident angle was selected as 0.8° and the step size of GI-XRD and XRR was 0.01° and 0.005°, respectively. The size of the mask on the incident beam was 10 mm for GI-XRD and 4 mm for XRR, and a 0.18° parallel plate collimator slit was used for the latter. The surface roughness of NMMs was measured using atomic force microscopy (AFM, Bruker) and the surface morphology and composition by a field-emission scanning electron microscopy (FE-SEM, LEO 1550) equipped with an Oxford INCASynergy energy dispersive X-ray spectroscopy (EDS). X-ray photoelectron spectroscopy (XPS, PHI Quantera SXM, USA) analysis was performed using Al  $K\alpha$  radiation source at constant pass energy of 69 eV, 0.125 eV step size and 25 total sweeps. Carbon 1s spectra at 285 eV was used for calibration. Transmission electron microscopy (TEM, JEOL 2100) was performed under 200 kV. TEM samples were prepared via the standard lift-out method using a focused ion beam microscopy (FIB, Helios600) with ~ 200 nm carbon coating followed by 2-3  $\mu$ m Pt protective coating.

# 2.2. Mechanical and tribological tests

Nanoindentation tests were performed by Hysitron Ti900 triboindenter using a standard Berkovich-type diamond tip following the Oliver and Pharr method [27]. A trapezoidal loading function with 5 sec loading/unloading time, 2 sec holding time, 4 and 5 mN maximum load was applied for all tests. The tip area function was calibrated using a standard fused quartz sample before indentation. The maximum load was chosen to ensure that the maximum penetration depth was less than ~ 15 % of the total film thickness in all tests to minimize the substrate effect [28]. All the reported results are the average of more than ten repeated tests for each sample sets. Nanowear tests were carried out by Hysitron Ti900 triboindenter over areas of 2  $\times$  2  $\mu$ m² on all samples using a standard conical-spherical diamond indenter at a constant nominal load of 90  $\mu$ N for up to 15 cycles. Hysitron Triboview software was used to determine the wear depth and worn area.

### 2.3. Corrosion and tribocorrosion tests

All electrochemical tests were conducted using Gamry Reference 600 potentiostat/galvanostat/ZRA. The effective exposed area was  $\sim 1~\rm cm^2$  on all specimens. Potentiodynamic polarization (PD) tests were carried out in naturally aerated 0.6 M NaCl aqueous solution (pH  $\sim 6.4~\pm~0.3)$  at ambient temperature using a three electrode cell where the specimen, activated titanium mesh, and a

commercial silver-silver chloride electrode (1 M KCl internal solution) served as the working (WE), counter (CE), and reference electrode (RE) respectively. Prior to the PD tests, open circuit potential (OCP) was stabilized for 5-10 min. The PD test started from  $\sim$  150 mV below OCP and terminated at  $\sim$  1.5 V above OCP, at a constant scan rate of 1 mV/s. The corrosion current densities (i\_corr) were evaluated by Tafel extrapolation over a linear portion of the polarization curve which is approximately 100 mV above and below OCP. Mott-Schottky analysis was performed from - 0.5 V vs. OCP to 1 V vs. OCP, by using 10 mV/s scan rate with a constant frequency of 1,000 Hz after stabilization for 30 min.

The tribocorrosion tests were conducted in 0.6 M NaCl aqueous solution at room temperature using a multifunctional tribometer (Rtec, CA, USA) [7]. The specimen (~ 1 cm² exposed area), mixed metal oxide coated titanium mesh, and Ag/AgCl electrode served as the WE, CE, and RE, respectively. An alumina ball (Al<sub>2</sub>O<sub>3</sub>, 4 mm diameter) was employed as the counterpart under a normal load of 0.5 N (or ~ 0.47 GPa contact pressure). Prior to each test, the OCP was stabilized for ~ 15 min. During the test, the specimen moves in linear reciprocal motion at a sliding velocity of 0.2 mm/s for 25 sec over a 5 mm scratch length. Each test was carried out using a new Al<sub>2</sub>O<sub>3</sub> ball to minimize contamination. After the tribocorrosion tests, the depth profile of wear tracks was measured by a Dektak XT profilometer. All electrochemical and tribocorrosion results reported were averaged from at least three separate tests under each test condition.

### 3. Computational methods

### 3.1. FE model geometry and meshing

A 2D finite element (FE) model was developed to study the tribocorrosion response of NMMs using COMSOL Multiphysics (version 5.3), as shown in Fig. 1(b). The geometry of the sample was simplified as a rectangle with ten layers, each of 3 nm thick, perfectly bonded while the effect of interface incoherency is not included for simplicity. The mechanical and electrochemical properties of the constituting materials were obtained from experiments. Due to the enormous difference in length scales for the tip (4 mm in diameter) and the nanolayers (3 nm in thickness), the tip was shrunk to ~ 20 nm diameter in the FE model and the applied load was concurrently decreased to 50 nN to ensure the same Hertzian contact pressure as the experiments. The indenter tip and NMMs were meshed with 0.25 nm element size, while the Si substrate, which has a stress distribution close to zero, was meshed with a coarse 0.5 nm size using triangular elements. All meshing sizes were chosen after convergence analysis. The FE simulation was performed for all NMMs under three scenarios: pure corrosion, pure wear, and tribocorrosion. Here, scratch wear was modeled as an indentation in the plane perpendicular to the wear track and friction perpendicular to the model plane is neglected for simplicity. According to Nelias et al. [29], when the friction coefficient is below 0.3, the frictional force does not significantly affect the subsurface stress level. Thus, scratch wear was simplified as an indentation in the plane perpendicular to the wear track and friction is neglected so that the model could be reduced to 2D to significantly save computation resource and time. The stress level under such load is quite low and the dominating wear mode will be ploughing [30], thus cutting and wedge formation is not included in this model for simplicity. Tribocorrosion of a single scratch stroke was modeled in two steps: (1) pure wear, and (2) corrosion of worn surface. Specifically, upon completion of step 1, the deformed surface geometry and residual subsurface stress and strain (after indenter unloading) were imported as the initial setup for step 2. The governing equations and boundary conditions are detailed in the Supplementary Materials. The mechano-electrochemical effect

was modeled as [31,32]  $\varphi_a = \varphi_{a0} - \frac{\sigma V_m}{zF} - \frac{TR}{zF} \ln K_\alpha(\varepsilon_p)$ , where  $\varphi_{a0}$ , the equilibrium anodic potential, was assumed to shift cathodically when subjected to stress  $\sigma$ . Here  $V_m$  is the molar volume of the corroding metal, z is the number of electrons involved in the reaction, F is Faraday's constant (96485 C/mol), T is the temperature (298 K), T is the ideal gas constant (8.3145 J/(mol·K), T is the effective plastic strain, and T is a function denoting the dislocation density increment under plastic strain (T in obtained by interpolating data from [33]. After the secondary current distribution (T in was calculated, the metal dissolution speed normal to the specimen surface was calculated according to Faraday's law as: T in T where T is the molar mass, T is the number of electrons involved in dissolving 1 metal atom and T is the density of the metal.

# 3.2. Density functional theory calculation

First-principles density functional theory (DFT) calculations were performed to determine the surface work function, oxygen (O) and chloride (Cl) adsorption energy for pure Al and Al/Ti NMM by using the Vienna ab initio simulation package (VASP) with the implementation of the projector augmented wave (PAW) pseudopotentials [34-36]. The Perdew-Burk-Ernzerhof (PBE) parameterization of the generalized gradient approximation (GGA) was used for exchange-correlation effects in the DFT calculations [37], with an energy cutoff of 450 eV and Methfessel-Paxton smear  $\sigma$  of 0.1 eV. For surface calculation, a 4 atomic layers slab was used for pure Al, Al/Ti, Al/Mg, and Al/Cu NMM with a vacuum layer of 15 Å above the metal. For pure Al and Al/Ti, the  $(5 \times 5 \times 1)$  Monkhorst-Pack mesh of k-points was used for Brillouin zone sampling [5,6], while  $(1 \times 1 \times 1)$  of Monkhorst-Pack mesh of k-points was used for Al/Mg and Al/Cu. This 4-layer model is confirmed to be adequate by comparing results with a 10-layer model (see Supplementary Materials Table S1). The constructed atomic structure was relaxed until the movement of each atom was less than 0.03 eV  $Å^{-1}$ . The criterion for convergence was set to be  $10^{-6}$  eV. During the optimization, the bottom layer of the metal was fixed while the top three layers were relaxed. Work function calculations were conducted with dipole correction if necessary.

# 4. Results

# 4.1. Microstructure characterization

Fig. 1(c) shows the GIXRD patterns of all as-deposited NMMs. In Al/Ti NMM, both face-centered-cubic Al (Fm3m) and hexagonal Ti (P6<sub>3</sub>/mmc) phases were detected. The high diffraction intensity at ~ 38.6° indicates the presence of strong Al (111) and Ti (0002) fiber texture in the film growth direction. In Al/Mg NMM, most diffractions were from hexagonal Mg phase (P6<sub>3</sub>/mmc) with only one diffraction from Al (220). A small hump around ~ 55.8° was also observed from the Si substrate. In Al/Cu NMM, in addition to the face-centered-cubic Cu phase (Fm3m), fcc Al diffractions were also detected. The presence of fewer diffractions of each phase than those of traditional polycrystalline metals is common for deposited thin films due to the presence of strong crystallographic texture, which formed during thin film growth as a result of surface and interface energy minimization, as well as strain-energy minimization [38,39].

XRR patterns of all samples are shown in Fig. 1(d). X-rays were completely reflected on each multilayer at increased critical angles of  $\sim 0.2^\circ,~0.25^\circ$  to  $0.32^\circ$  for Al/Mg, Al/Ti, and Al/Cu NMMs respectively, in agreement with their increasing density from Al/Mg ( $\rho_{\rm Al/Mg}\approx 2.22~\rm g/cm^3$ ), Al/Ti ( $\rho_{\rm Al/Ti}\approx 3.6~\rm g/cm^3$ ), to Al/Cu ( $\rho_{\rm Al/Cu}\approx 5.83~\rm g/cm^3$ ). With the angle increase, the reflective intensity is

weakened until the appearance of Bragg peaks because of interfacial roughness between the layers. However, there is no obvious oscillation before reaching the Bragg peaks, probably due to the extremely small layer thickness or surface roughness [40,41]. The bi-layer periodicity (d =  $h_{Al}$  +  $h_{x}$ ) can be calculated by d =  $2\pi/q$  [42,43], where the lattice vector q can be obtained from the Bragg angle  $\theta$  following the equation q= $4\pi \sin\theta/\lambda$ . Table 1 summarizes the calculated d, which is ~ 6 nm for all samples.

All as-deposited samples appear mirror-finish to naked eye. SEM images in Fig. 2(a)-(c) show only nanoscale surface nodules on all samples. AFM analysis in Fig. 2(d)-(f) revealed the arithmetic average roughness (Ra) of all NMMs was ~ 4.4-5.5 nm. The directly measured bi-layer thicknesses from TEM results are listed in Table 1, in good agreement with x-ray results. Fig. 2(g) shows typical bright-field TEM image of Al/Ti NMM, where the film growth direction aligns with Al [111]. Semi-coherent interfaces were observed between the Al and Ti layers, with the orientation relationship of Al $\{111\}$  || Ti $\{2000\}$  and Al $\langle110\rangle$  || Ti $\langle1120\rangle$ . Bright-field TEM image (Fig. 2(h) inset) shows that there is no detectable phase contrast between the Al and Mg layers in Al/Mg NMMs, likely due to their similar atomic weight and epitaxial growth. Inverse FFT image of Al/Mg NMM in Fig. 2(h) shows the presence of largely coherent interfaces between the Al and Mg layers, with an orientation relationship of (110)Al | (1011)Mg, resulting in an in-plane strain of ~ 14.5%. Fig. 2(i) shows the orientation relationship of Cu{111} || Al{200} parallel to the film growth direction in Al/Cu NMM, in agreement with the x-ray results (Fig. 1(c)). Additional high resolution TEM analysis (results not shown here) shows the interfaces in Al/Cu are semi-coherent. The grain sizes (d) of all NMMs were estimated by the linear intercept method from TEM images to be 178.5  $\pm$  13.3 nm for Al/Ti, 127.6  $\pm$  16.1 nm for Al/Mg, and 74.5  $\pm$  15.2 nm for Al/Cu NMMs. Given that in all NMMs, d is much bigger than h (3 nm), it is assumed that the dominating structural length scale for mechanical properties is h [44].

### 4.2. Mechanical and wear properties

The hardness (H) and elastic modulus (E) of all NMMs measured by nanoindentation tests are summarized in Fig. 3(a) and Table 1. For comparison, the mechanical properties of monolithic films measured using the same method are listed in Table 2. SEM images of typical indents on all NMM samples can be found in Fig. S1(a-c) in the Supplemental Materials. No surface crack or apparent pile-up was observed in all samples after nanoindentation, indicating relatively high strength and strain hardening exponent [45]. Results in Tables 1 and 2 show that the hardness of all NMMs is ~ 3-5 times greater than their corresponding rule-of-mixture hardness H<sub>ROM</sub>, similar to those reported previously [46,47]. Interestingly, pure Ti film is harder than pure Cu film, yet Al/Cu NMM is harder than Al/Ti NMM. It is also noted that the presence of any potential residual stress could also affect the hardness and other properties of NMMs, the measurement and analysis of which is left for future work.

Nanowear tests were carried out on all NMM samples under a constant load of 90  $\mu$ N for up to 15 cycles. Fig. 3(b) shows that the wear rates (i.e. total volume loss normalized by the number of cycles) decreased with the number of cycles due to subsurface work-hardening until reaching a quasi-steady state after ~ 10 cycles, during which Al/Cu and Al/Mg NMMs exhibit the lowest and highest wear rate respectively. Fig. 3(d)-(f) show the typical surface topographies after 10 cycles. The corresponding surface height profiles and wear properties are summarized in Fig. 3(c) and Table 3 respectively. Al/Cu NMMs exhibited the best wear resistance due to their highest hardness, in consistent with the Archard's law [13]. However, a deviation from this behavior was observed during the running-in period (at two cycles of wear), probably due to the

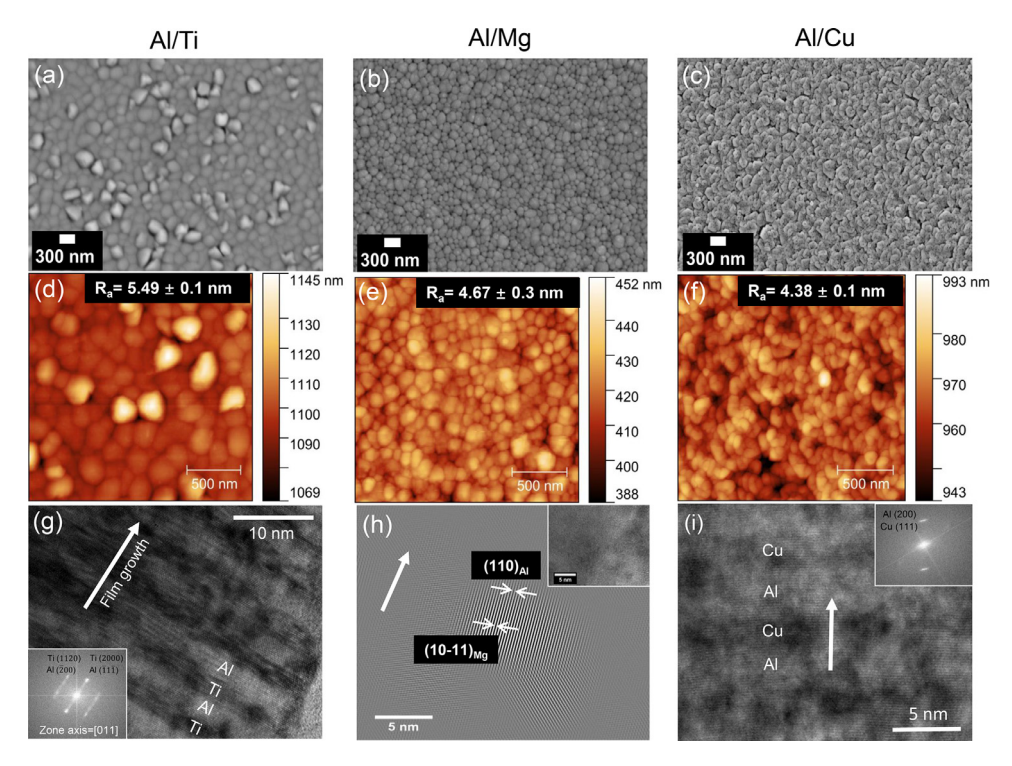
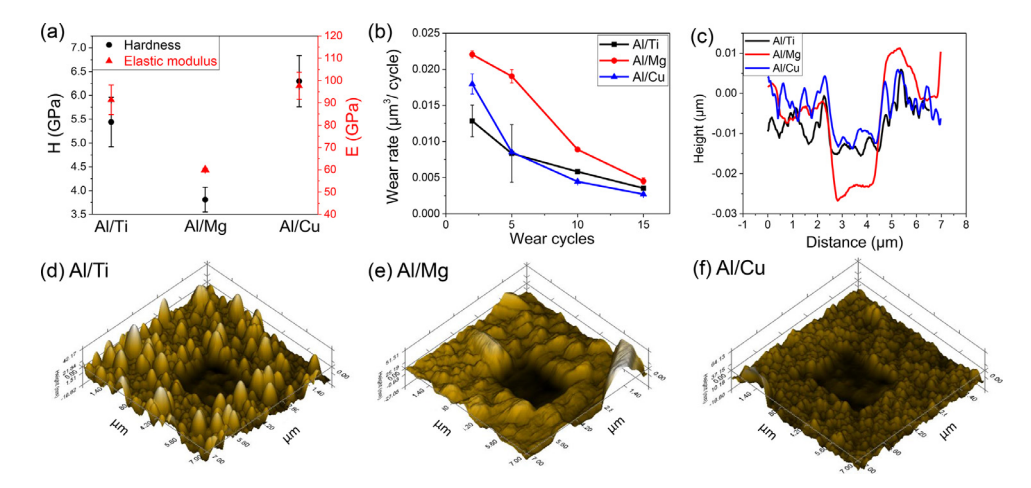


Fig. 2. (a-c) SEM, (d-f) AFM, (g), (i) bright-field TEM, and (h) inverse FFT TEM images of NMMs. Arrows in (g-i) indicate film growth direction. Insets in (g) and (i) are FFT images of the corresponding TEM images, while that in (h) is the corresponding bright-filed TEM image.



**Fig. 3.** (a) Mechanical properties and (b) wear rates as a function of number of cycles for all NMM samples. (c) Surface height profiles and (d)-(f) surface topographies of all NMM samples after 10 cycles of wear under 90  $\mu$ N.

**Table 3**Summary of wear, corrosion, and tribocorrosion properties of all Al/X NMM samples. Wear test data were taken from all samples after 10 cycles of wear. Each value is reported as average and standard deviation from at least three separate tests.

Sample ID	Wear			Corrosion		Tribocorrosion		
	D (× 10 <sup>-4</sup> mm)	W (× 10 <sup>-3</sup> mm)	V (× 10 <sup>-11</sup> mm <sup>3</sup> )	E <sub>corr</sub> (V vs. Ag/AgCl)	i <sub>corr</sub> (μA/cm <sup>2</sup> )	D (× 10 <sup>-4</sup> mm)	W (mm)	V (× 10 <sup>-6</sup> mm <sup>3</sup> )
Al/Ti Al/Mg Al/Cu	$\begin{array}{c} 0.15\pm0.006 \\ 0.22\pm0.005 \\ 0.11\pm0.006 \end{array}$	$\begin{array}{c} 2.4 \pm 0.1 \\ 2.6 \pm 0.1 \\ 2.3 \pm 0.05 \end{array}$	$\begin{array}{c} 5.81\pm0.24 \\ 8.89\pm0.23 \\ 4.44\pm0.24 \end{array}$	$\begin{array}{l} -0.62\pm0.17 \\ -1.7\pm0.04 \\ -0.28\pm0.01 \end{array}$	$\begin{array}{c} 0.041 \pm 0.02 \\ 3.89 \pm 1.2 \\ 1.55 \pm 0.94 \end{array}$	$\begin{array}{c} 1.21  \pm  0.92 \\ 5.87  \pm  0.51 \\ 0.17  \pm  0.017 \end{array}$	$\begin{array}{c} 0.014 \pm 0.001 \\ 0.049 \pm 0.01 \\ 0.031 \pm 0.003 \end{array}$	4.88 ± 2.52 144 ± 42.4 2.54 ± 0.10

different surface roughness of Al/Ti and Al/Cu. Higher roughness in Al/Ti leads to a smaller real contact area, hence lower material loss than that of Al/Cu NMM.

# 4.3. Corrosion behavior

Fig. 4(a) and (b) present the typical Tafel plots of all samples after PD tests in 0.6 M NaCl aqueous solution at room temperature.

The measured  $E_{corr}$  and  $i_{corr}$  are summarized in Tables 2 and 3. It is noted here while current rather than current density was preferred for Tafel plots of galvanic couples, in the present work, each NMM sample is treated as a 'composite' material and the measured current density is calculated by normalizing the corrosion current by the exposed sample area. In Fig. 4(a),  $E_{corr}$  of monolithic Ti and Cu are more positive while that of Mg more negative than that of Al, which is in agreement with previous results [48–50]. The

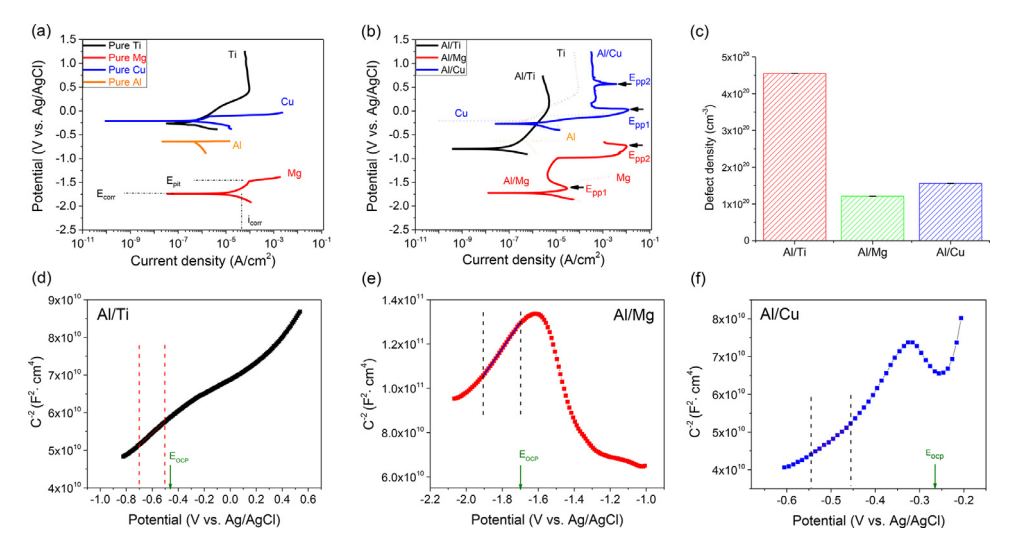


Fig. 4. Typical potentiodynamic polarization curves of (a) monolithic films and (b) NMMs in 0.6 M NaCl solution at room temperature. Results in (a) are replotted as dashed lines in (b) for direct comparison. (d-f) Mott–Schottky plots and (c) n-type defect density of all NMMs.

values of  $E_{corr}$  increase in the order of Mg, Al, Ti, and Cu, in consistent with their reduction potential trend from the EMF series under the standard state.  $i_{corr}$  is the smallest for pure Ti and highest for Mg. Among all monolithic samples, Al exhibited active corrosion in the anodic branch, Cu and Mg exhibited pitting behavior at  $E_{pit}$ , while Ti exhibited an active-pseudo passive behavior, with a transition potential around 0.4 V vs. Ag/AgCl.

Fig. 4(b) shows that the i<sub>corr</sub> of all NMM samples increases in the order of Al/Ti, Al/Cu, and Al/Mg while Ecorr increases in the order of Al/Mg, Al/Ti, and Al/Cu. The anodic polarization branches of all NMMs are characteristically different. For both Al/Mg and Al/Cu NMMs, an active-passive type of behavior was observed, where the anodic corrosion current density first increased with potential from E<sub>corr</sub>, then reversed to a lower value over a range of more positive potentials. Interestingly, for both samples, two primary passive potential  $E_{DD}$  was observed, at ~ -1.62 V and ~ -0.74 V vs. Ag/AgCl for Al/Mg NMMs, and ~ 0.03 V and 0.57 V vs. Ag/AgCl for Al/Cu NMMs. Such behavior is likely due to the switching of corrosion mode between a passive state, contributed mainly by the outmost Al layer, and an active corrosion state by the underneath Mg and Cu layers as corrosion progressed through the thickness of the NMMs. On the other hand, the anodic branch of Al/Ti exhibited a stable passive state over the majority of the anodic potential with icorr of  $\sim 0.042~\mu\text{A/cm}^2$ , smaller than that of either Al or Ti. This i<sub>corr</sub> value is around two orders of magnitude smaller than those reported of Al/Ti bilayers and multilayers with micrometer-sized individual layer thickness [51,52].

Mott-Schottky (MS) results are shown in Fig. 4(c-f). The capacitance of the Helmholtz layer is assumed to be much bigger than the semiconductor capacitance of the passive layer, hence the measured capacitance C is taken as the semiconductor capacitance of the passive layer to calculate the defect densities according to [53,54]  $\frac{1}{C^2} = \frac{\pm 2}{\epsilon \cdot \epsilon_0 \cdot q \cdot N} \times (E - E_{fb} - \frac{kT}{q})$ , where  $\epsilon$  is the passive film dielectric constant (10 for  $Al_2O_3$ ),  $\epsilon_0$  is the permittivity of vacuum ( $\epsilon_0$ =8.85 ×  $10^{-14}$  F/cm), N is the donor or acceptor density,  $E_{fb}$  is the flat band potential, k is the Boltzmann constant (1.38 ×  $10^{-23}$  JK<sup>-1</sup>), T is the absolute temperature, and q is the elementary charge (1.602 ×  $10^{-19}$  C). According to this relationship, a positive slope of the MS curve indicate the presence of n-type defect such as oxygen vacancies and cation interstitials (e.g.  $Al^{3+}$ ), while a negative slope indicates p-type defect such as cation vacancies. Fig. 4 shows that while only n-type defects are present in Al/Ti over the whole potential range, both Al/Mg and Al/Cu experiences a transition from n-type to p-type when the potential

increases above OCP. It is likely the active corrosion of Mg and Cu in the later lead to the dissolution of metallic ions at the surface, leaving behind cation vacancies. Fig. 4(c) shows the n-type defect density of all NMMs measured from the cathodic potential region (between the dashed lines in Fig. 4(d-f)), hence corresponds to that of the intact surface Al layer. It can be seen that the defect density of all samples is ~ 10<sup>20</sup> /cm³, with Al/Ti slightly higher than the rest. These values are about two orders of magnitude lower than those measured in pure Al and Al 3003 alloy [53].

The corroded surface morphology and elemental mappings were shown in Fig. 5(a-c), which are in good agreement with their PD results. The corroded surface of Al/Ti NMM (Fig. 5(a)) resembled that of the as-deposited sample, confirming its lack of either active or localized corrosion. On the other hand, the majority of Al/Mg NMM is gone after PD tests, as shown in Fig. 5(b), exposing large areas of Si substrate. On the corroded surface of Al/Cu, extensive nanometer-sized nodules could be seen, as marked by arrow in Fig. 5(c). EDS mapping in Fig. 5(c) suggests that these nodules are enriched in Cu. Similar surface enrichment of Cu has also been reported in Al-Cu-Li [55] and Al-Cu [56] alloys, due to dealloying of copper-rich inclusions being redistributed on the aluminum surface.

### 4.4. Tribocorrosion behavior

Fig. 6(a) shows the typical OCP evolution of all samples during tribocorrosion tests in 0.6 M NaCl solution. In all samples, OCP shifted to the cathodic direction upon getting in contact with the counter body at the beginning of the test, and restored the original value once the test was ended. The magnitude of this cathodic potential shift was large for Al/Ti NMM (~ 86 mV) and quite small for Al/Mg (~ 8 mV) and Al/Cu NMM (~ 1.6 mV). This observation is consistent with the PD corrosion results, where unlike Al/Mg and Al/Cu, passivity, instead of galvanic corrosion, was dominating in Al/Ti. During tribocorrosion, the mechanical removal of the protective passive film by the counter body, i.e. the depassivation process, led to the shift of the corrosion potential in the more active direction. Once the test was finished, OCP shifted back to its original steady state value, indicating a repassivation of the worn area. On the other hand, the small potential shift of Al/Mg and Al/Cu indicates a lack of surface passivity. Hence depassivation by the counter body has small effect on OCP. The repassivation time, i.e. the time required for OCP to restore its initial value at the end

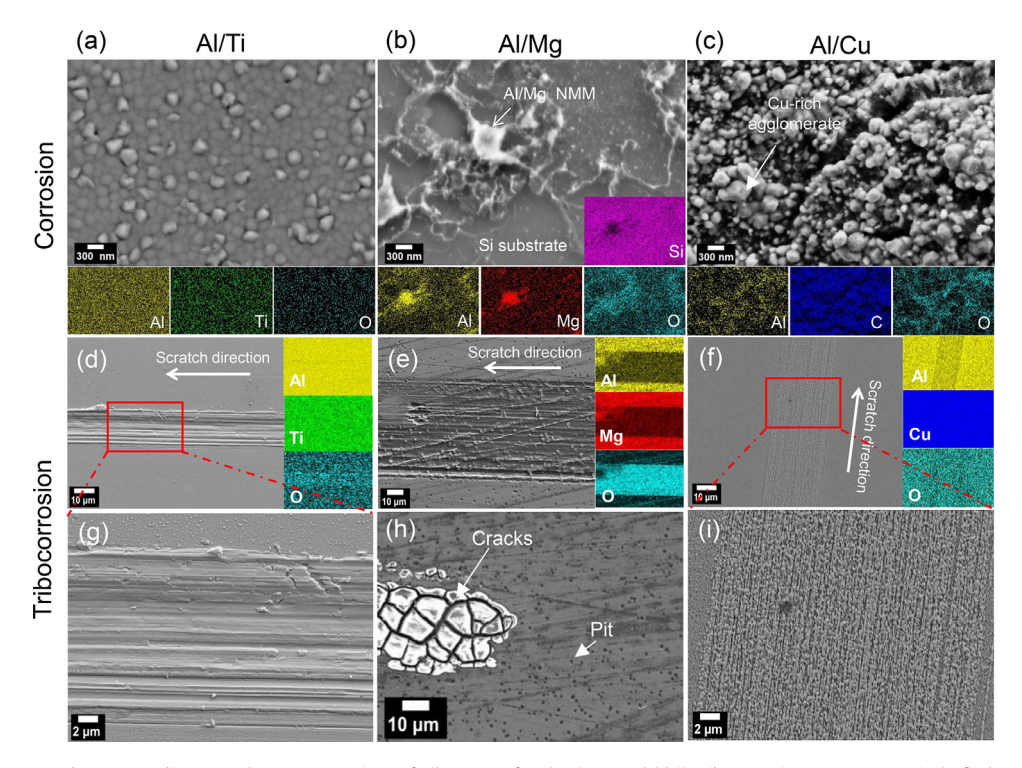
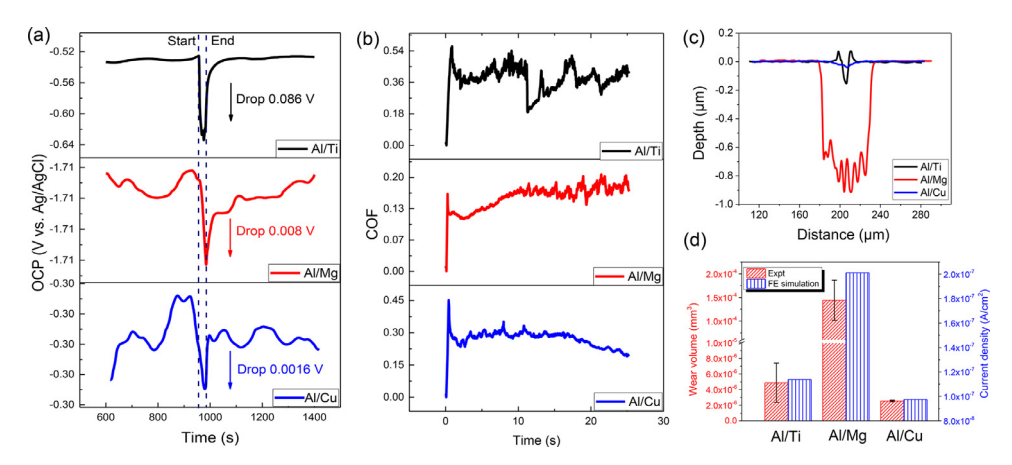


Fig. 5. Surface SEM images and corresponding EDS elements mappings of all NMMs after (a-c) PD and (d-i) tribocorrosion tests. Inserts in (a-f) show the corresponding EDS element maps.



**Fig. 6.** Evolution of (a) open circuit potential, (b) coefficient of friction (COF) of all multilayers during tribocorrosion tests. (c) Typical wear track cross-sectional surface depth profiles and (d) summary of experimentally measured wear volume and FE model predicted corrosion current of all NMMs after tribocorrosion tests. The profiles in (c) were measured perpendicular to the sliding direction on the worn surface of all samples.

of the test was ~ 73 s for Al/Ti, followed by ~ 82 s for Al/Cu and ~ 388 s for Al/Mg. As a comparison, the repassivation time of pure Al film is ~ 45 s from [7], much shorter than that of all NMMs, likely due to its chemical homogeneity. Coefficient of friction (COF) of all samples was presented in Fig. 6(b). Al/Ti NMM exhibited the highest average COF ( $\sim$  0.38), followed by Al/Cu ( $\sim$  0.27) and Al/Mg ( $\sim$  0.16). Fig. 6(c) and (d) show the wear track profiles and total material volume loss of all NMMs after tribocorrosion tests respectively. Among all samples, the wear track of Al/Mg NMM was the widest and deepest, in agreement with their low hardness and high corrosion rate. Al/Cu NMM exhibited the smallest material loss, hence the best tribocorrosion resistance, most likely due to its highest wear resistance. Al/Ti NMM, although showing the highest corrosion resistance, was slightly inferior to Al/Cu under the chosen tribocorrosion testing condition. It should also be pointed out that if a different tribocorrosion condition was chosen so that the mechanical wear occurs at a much smaller frequency

than those conducted here, Al/Ti will be expected to be the most tribocorrosion-resistant since material loss will be dominated by corrosion and less frequently by wear.

# 4.5. Surface chemistry and microstructure after tribocorrosion

Fig. 5(d-i) shows the surface morphologies and corresponding EDS mappings of all NMM samples after tribocorrosion tests. The wear track of Al/Ti NMMs is characterized by deep grooves and high pile-ups near the edge of the track, suggesting largely abrasive wear during scratch. The inset EDS mappings in Fig. 5(d) show uniform distribution of Al and Ti elements in either the worn or unworn area with a higher O composition within the wear track (~ 2.36 at%) than that outside (~ 0.84 at%). This observation is consistent with prior corrosion and tribocorrosion results, indicating the formation of a protective (hydr)oxide layer on the wear track. For Al/Mg NMM, EDS analysis in Fig. 5(e) inset revealed that the

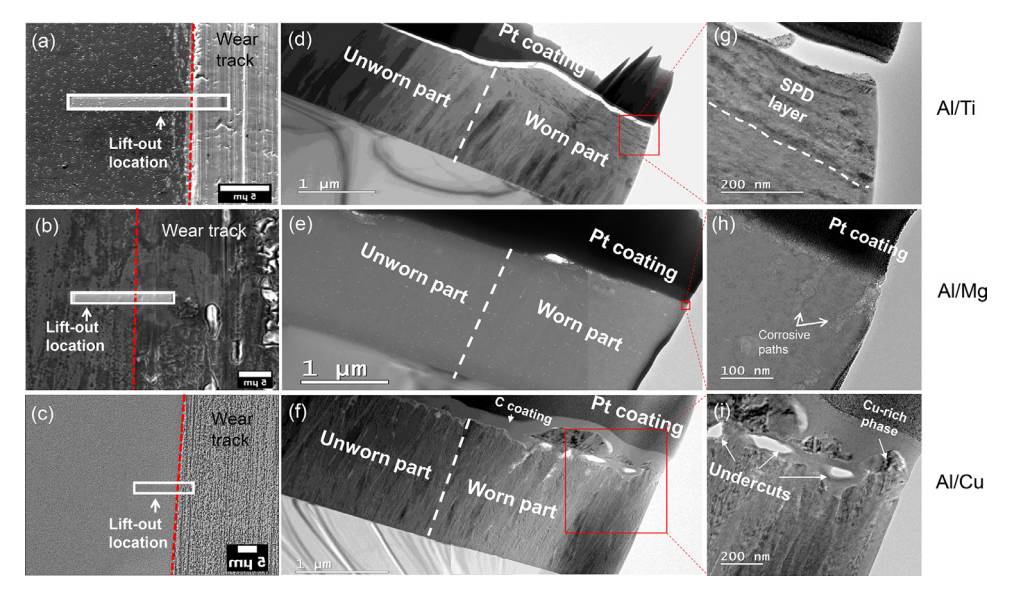


Fig. 7. (a-c) Surface SEM images and (d-i) cross-sectional bright-field TEM images of all NMMs after tribocorrosion tests.

majority of the sample was removed in the worn area, leaving behind a high O concentration most likely from SiO2 layer on the Si substrate. Within the wear track, in locations where the NMM is still present (Fig. 5(h)), extensive cracks were seen on the tribocorroded surface, similar to dehydration cracks formed on corrosion products of many Mg alloys [57]. Away from the wear track, extensive pits were seen, of ~ 200 - 600 nm diameter. For Al/Cu NMM, Fig. 5(f) and (i) show that its wear track has extensive fine scratch lines along the sliding direction. In addition, the wear track contains high nanoscale surface roughness with higher Cu concentration than the rest of the sample. This partial dissolution of Al in Al/Cu NMM could be related to the anodic nature of Al in the Al-Cu galvanic couple, in consistent with those observed after pure corrosion (Fig. 5(c)). The surface morphology and EDS analysis far away from the wear track of all NMM samples after tribocorrosion tests are presented in the Supplemental Materials Fig. S2, which are similar to those observed during pure corrosion (Fig. 5(a-c)). Additional XPS analysis (Supplemental Materials Figs. S3) indicate that in all as-deposited samples, the surface contains mainly alumina (Al<sub>2</sub>O<sub>3</sub>) and metallic forms of Al and X (X=Ti, Mg, and Cu), as expected [58]. Al<sub>2</sub>O<sub>3</sub> is also the main surface component after tribocorrosion in all samples. In Al/Mg NMM, Mg(OH)<sub>2</sub> was also detected from both the worn and unworn areas, resulting from active corrosion of Mg. In both Al/Cu and Al/Ti NMMs, no copper oxide or titanium oxide was detected, likely due to the cathodic protection provided by the more active Al layers [26].

Fig. 7(d-i) show TEM images of the tribocorroded NMMs. Plastic deformation dominates the subsurface of Al/Ti NMM and a severe plastically deformed (SPD) layer of ~ 450 nm was formed, where extensive shear-induced mixing erased the well-defined interface contrast between the Al and Ti layers. On the other hand, corrosion degradation instead of plastic deformation dominates the worn surfaces of Al/Mg (Fig. 7(e,h)) and Al/Cu (Fig. 7(f,i)). It is noted here that within the wear track of Al/Mg, most of the film was gone (see Fig. 5(e)), and the TEM lift-out was performed at a location where the film was still present. In Al/Mg NMM, deep and narrow corrosion paths can be seen, extending a few hundred nm deep below the surface. In Al/Cu NMM, frequent undercuts can be seen under the Cu-rich phases that were redeposited on the surface after Al dissolution.

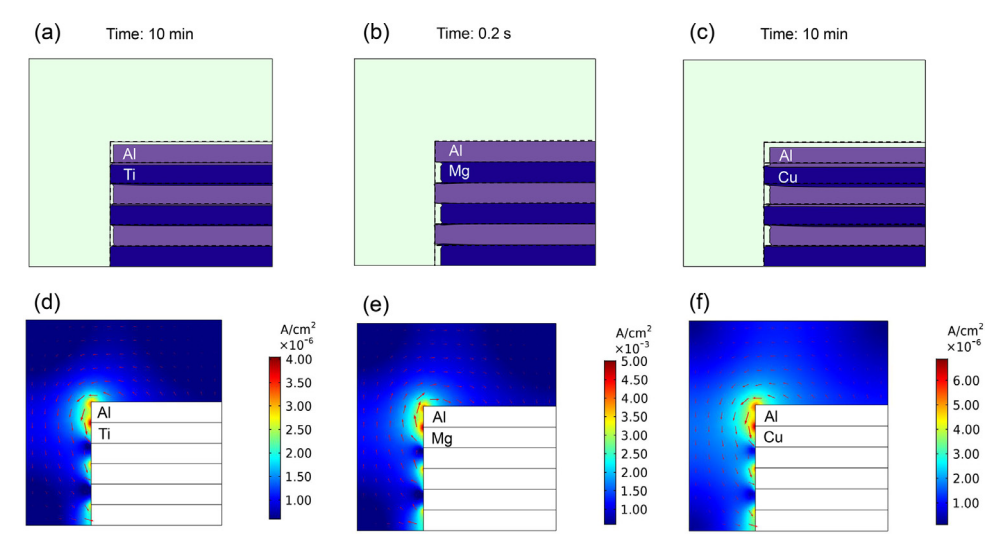


Fig. 8. FE model results of (a-c) cross-sectional morphology and (d-f) current density distribution of all NMMs after corrosion in 0.6 M NaCl aqueous solution.

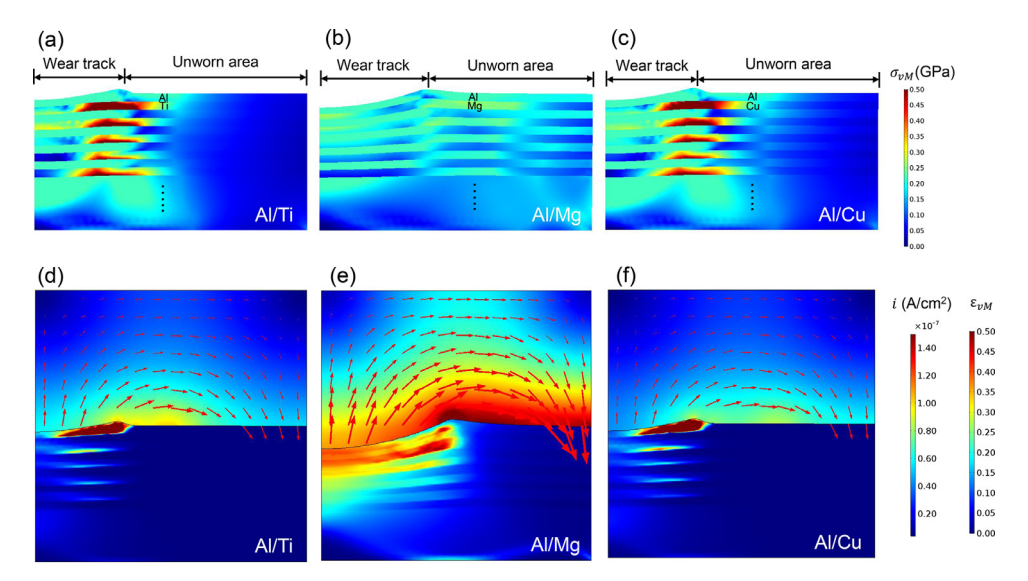


Fig. 9. FE simulation results of (a-c) von Mises stress distribution after wear, and (d-f) von Mises strain and current density distribution after tribocorrosion in 0.6 M NaCl aqueous solution of all NMMs.

# 4.6. FE simulation results

FE simulation results are presented in Figs.8,9. Fig. 8(a)-(c) show the corroded morphology and Fig. 8(d)-(e) the corresponding current density distribution of each sample after pure corrosion for 0.2 s (Al/Mg) or 10 min (Al/Ti and Al/Cu), where both the surface and the cross-section are in contact with the electrolyte. Exposing the cross-sections to the electrolyte allows the study of the corrosion behavior once pitting occurs at the surface, exposing the underneath layers. Dashed lines present the original surface position before corrosion. The corrosion of Al/Mg NMM is very rapid and leads to extremely irregular geometry and challenges model convergence over long immersion time, so it is only simulated for 0.2 s here (Fig. 8(b)). As is evident from cross-sectional morphology and current density distribution, Al layers act as sacrificial anode layers in Al/Ti and Al/Cu NMM systems and the total corrosion happens at a slow rate, while Al/Mg corrodes very fast with Mg as the anode layers. Among all samples, Al/Ti exhibited the smallest material loss while Al/Mg exhibited the largest material loss, in agreement with those measured experimentally. Remarkably, anode layers adjacent to the interface were subjected to severe galvanic corrosion attack causing more material loss while little change occurred on the cathode layers, suggesting better protection for cathode layers in the interface areas. Similarly, results in Fig. 8(d-e) show that the current density is concentrated at the interfaces, particularly in the top two layers, and gradually lowers in interfaces farther away.

Fig. 9(a-c) show the subsurface stress distribution of all samples after pure wear. The residual contact size is the largest of Al/Mg NMMs, in agreement with Hertzian contact theory predictions and experimental observations in Fig. S1. In all NMMs, the stiffer layers (e.g. Ti in Al/Ti) experienced higher stress than the more compliant ones during co-deformation. Fig. 9(d-f) show the surface current density distribution as well as subsurface residual strain of all NMMs during tribocorrosion. The worn area surfaces suffer from a higher dissolution rate than the unworn areas and dissolution rate reaches a maximum at the wear track edge. Notably, galvanic coupling is established between the worn region as anode and undeformed region as cathode, resulting in corrosion acceleration within the wear track. The thicknesses of arrows in Fig. 9(d-f) is proportional to the corrosion current density, which is highest for Al/Mg and lowest for Al/Cu, in agreement

with the experimentally measured wear volume trend, as shown in Fig. 8(d).

### 5. Discussion

According to the mixed potential theory (MPT) [26], the corrosion potential of a galvanic couple A/B ( $E_{corr}^{A/B}$ ) is always in between those of uncoupled metal A ( $E_{corr}^{A}$ ) and B ( $E_{corr}^{B}$ ), and at potentials cathodic to  $E_{corr}^{A/B}$ , the cathodic current of the couple should be deminated by the core with higher cathodic ple should be dominated by the one with higher cathodic current, likewise for the anodic current. In the present study, this was indeed the case for Al/Mg and Al/Cu NMMs. For example, in Al/Cu NMM,  $E_{corr}^{Al/Cu}$  is in between that of  $E_{corr}^{Al}$  and  $E_{corr}^{Cu}$  (Fig. 4(b)). In addition, the cathodic branch of the Al/Cu PD curve is similar to that of Cu. However, a deviation from MPT was observed for Al/Ti NMM, where both the cathodic and anodic current of the couple was about one order of magnitude smaller than that of either uncoupled Al or Ti. The cathodic reaction during corrosion under this potential range, is assumed to be dominated by hydrogen reduction as  $2H^+ + 2e^- \rightarrow H_2$ . A reduction of cathodic reaction rate of Al/Ti NMM indicates a reduction of the exchange current of hydrogen reaction  $(i_{0,H^+/H_2})$  on the surface. Likewise, the reduction of anodic reaction rates indicates a reduction of  $i_{o,Al^{3+}/Al}$  in the anodic reaction  $2Al + 3H_2O \rightarrow Al_2O_3 + 6H^+ + 3e^-$ . The fact that both cathodic and anodic kinetics is smaller on Al/Ti NMM than those on monolithic Al, whose outmost surface is the same, indicates that the nanolayered strategy is reducing the surface activity.

To understand the atomic origin of such behavior, DFT calculations were carried out to evaluate the work function (WF), oxygen (O) and chloride (Cl) adsorption energies of Al/Ti NMM and pure Al, which are directly related to the corrosion and pitting resistance of the metal surface. Fig. 10(a-b) show that the WF of Al and Al/Ti NMM is 4.04 eV and 4.19 eV, respectively. Since WF is defined as the work needed to remove an electron from the surface, a higher WF indicates it is more difficult to lose electrons at the surface, hence reduced surface activity. In this case, Al/Ti NMM has a higher WF, showing potential for better corrosion resistance compared to Al, in agreement with those observed experimentally.

Finally, the O and Cl adsorption energies ( $E_{ad}^{Oxy}$  and  $E_{ad}^{Cl}$ ) were calculated as [59]:

$$E_{ad}^{Oxy} = E_{M-Oxy} - E_M - \frac{1}{2}E_{O_2}, \tag{7}$$

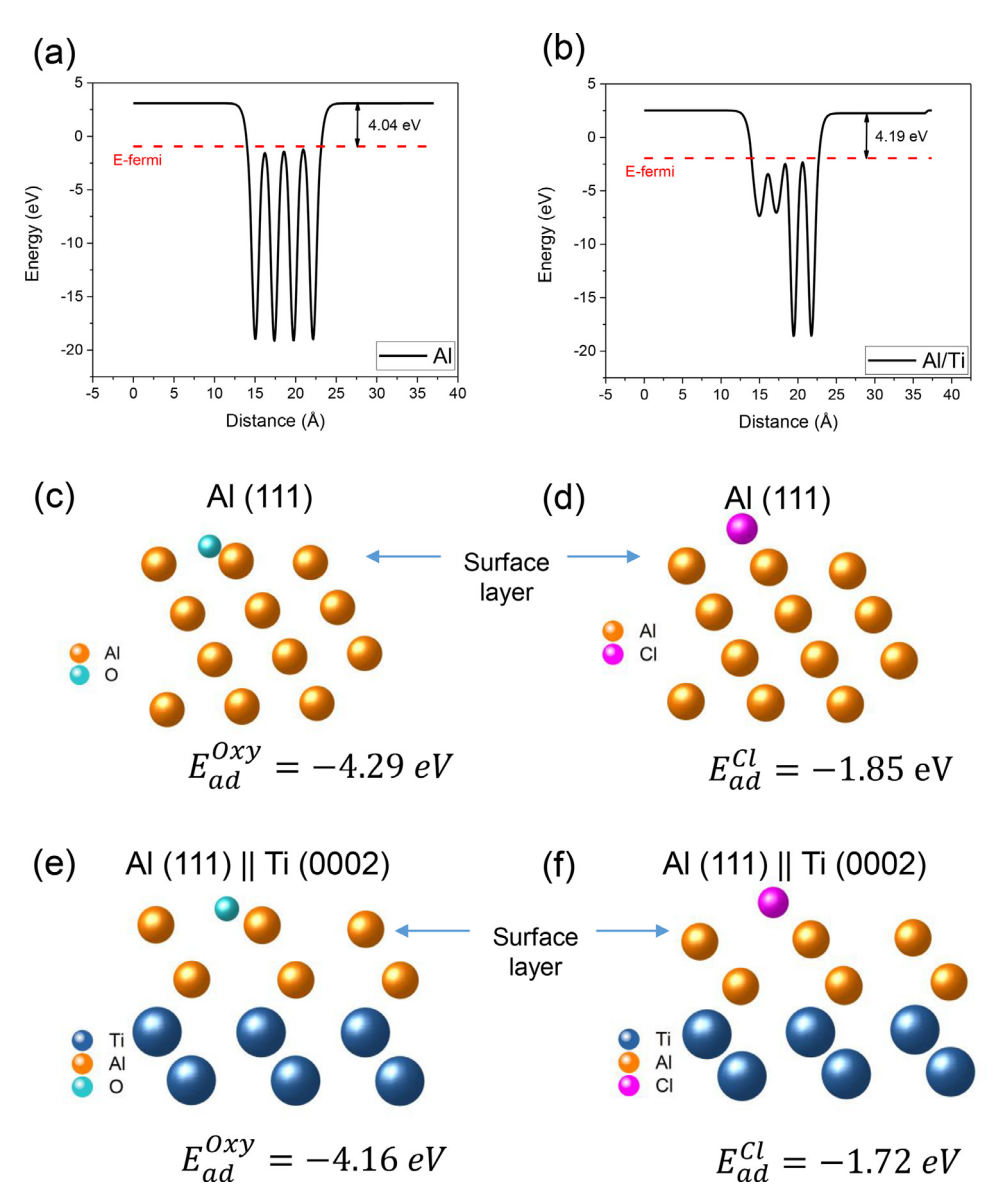


Fig. 10. Calculated (a-b) work function of, (c, e) O and (d, f) Cl adsorption on Al (111) and Al/Ti NMM with Al(111) || Ti(0002).

and

$$E_{ad}^{Cl} = E_{M-Cl} - E_M - \frac{1}{2} E_{Cl_2}, \tag{8}$$

where  $E_{\rm M}$  is the energy of clean metal surface,  $E_{\rm O_2}$  and  $E_{\rm Cl_2}$  is the energy of  $O_2$  and  $Cl_2$  molecule respectively, and  $E_{M-Oxy}$  and  $E_{M-Cl}$  is the energy of O and Cl bonded metal surface respectively. Adsorption of O and Cl on Al and Al/Ti NMM are illustrated in Fig. 10 (c-f), with fcc hollow site as the most favorable adsorption site and a coverage of 0.25 ML. The O adsorption energy on Al and Al/Ti NMM surface are -4.29 eV and -4.16 eV respectively, with a very small difference of 3.1% between the two, while that of Cl adsorption shows a 7.6% difference on Al (-1.85 eV) and Al/Ti (-1.72 eV). These results indicate that the nanolayering strategy not only reduced surface activity of Al, but also reduced its tendency to adsorb the aggressive Cl ions from the environment, thereby enhancing the overall corrosion resistance. Additional calculations on Al/Mg and Al/Cu NMMs (see Supplementary Materials Table S2 and Fig. S4) show that among all NMMs, Al/Ti NMM has the least negative adsorption energy for both O and Cl, in agreement with its best corrosion resistance among all NMMs observed experimentally.

### 6. Conclusions

A synergistic experimental and computational study was carried out to evaluate the effects of constituting materials on the tribocorrosion behavior of Al/X NMMs. It was found experimentally that the degradation and deformation mode of Al/X depends on both of their mechanical and electrochemical properties. While plastic deformation and wear rely heavily on stiffness mismatch between the constituents and the interface coherency, corrosion behavior was more complicated. In Al/Mg and Al/Cu NMMs where Al is the only passive element, micro-galvanic corrosion dominates material loss, as predicted from the mixed potential theory. On the other hand, in Al/Ti NMM where both constituents are passive metals, Al is the only specie that participates in the passive film formation during corrosion and tribocorrosion despites the wide passivity window of Ti. FE simulations confirm that galvanic corrosion dominates material loss in NMMs, resulting in accelerated material loss in the anode layers near the top interfaces. By considering material loss due to wear, corrosion, as well as stressaccelerated corrosion, the developed FE model successfully predicted the trend of tribocorrosion rate of all NMMs, in agreement

with experimental observations. Finally, DFT simulations were carried out to understand the atomic origin of the high corrosion resistance of Al/Ti NMM. It was found that by nanolayering with Ti, the surface work function of Al is increased while Cl adsorption energy decreased, resulting in a less active surface with reduced corrosion susceptibility.

### **Declaration of Competing Interest**

The authors declare that they have no known competing financial interests or personal relationships that could have appeared to influence the work reported in this paper.

#### Acknowledgements

This research was financially supported by the US National Science Foundation under Grant CMMI-1855651 and DMR-1856196. X-ray diffraction measurements were conducted at the Virginia Tech Crystallography (VTX) Lab with support from the Virginia Tech National Center for Earth and Environmental Nanotechnology Infrastructure (NanoEarth, NSF Cooperative Agreement 1542100). W.W. gratefully acknowledge the discussion of XPS analysis and results with Dr. Weinan Leng, and assistance with FIB sample preparation from Ya-peng Yu of the Nanoscale Characterization and Fabrication Laboratory at Virginia Tech. The computational resource used in this work is provided by the advanced research computing at Virginia Polytechnic Institute and State University.

# Supplementary materials

Supplementary material associated with this article can be found, in the online version, at doi:10.1016/j.actamat.2020.116609.

### References

- [1] D. Landolt, S. Mischler, M. Stemp, Electrochemical methods in tribocorrosion: a critical appraisal, Electrochimica Acta 46 (24-25) (2001) 3913–3929.
- [2] K. Pondicherry, D. Fauconnier, P. De Baets, Synergism in multi-asperity abrasion-corrosion of martensitic and dual phase steels in three aqueous electrolytes, Wear (2020) 452.
- [3] S. Roy, J.M. Coyne, J.A. Novak, M.A. Edwards, Flow-induced failure mechanisms of copper pipe in potable water systems, Corros Rev 36 (5) (2018) 449–481.
- [4] Y.S. Kim, S.K. Lee, H.J. Chung, J.G. Kim, Influence of a simulated deep sea condition on the cathodic protection and electric field of an underwater vehicle, Ocean Eng 148 (2018) 223–233.
- [5] M. Buciumeanu, A. Bagheri, J.C.M. Souza, F.S. Silva, B. Henriques, Tribocorrosion behavior of hot pressed CoCrMo alloys in artificial saliva, Tribol Int 97 (2016) 423–430.
- [6] H. Mraied, W. Wang, W. Cai, Influence of Chemical Heterogeneity and Microstructure on the Corrosion Resistance of Biodegradable WE43 Magnesium Alloys, Journal of Materials Chemistry B (2019).
- [7] H. Mraied, W.J. Cai, The effects of Mn concentration on the tribocorrosion resistance of Al-Mn alloys, Wear 380-381 (2017) 191–202.
- [8] T.T. Xie, S.D. Mao, C. Yu, S.J. Wang, Z.L. Song, Structure, corrosion, and hardness properties of Ti/Al multilayers coated on NdFeB by magnetron sputtering, Vacuum 86 (10) (2012) 1583–1588.
- [9] J. Creus, E.H. Top, C. Savall, P. Refait, C. Ducros, F. Sanchette, Mechanical and corrosion properties of dc magnetron sputtered Al/Cr multilayers, Surf Coat Tech 202 (16) (2008) 4047–4055.
- [10] A. Misra, J.P. Hirth, R.G. Hoagland, Length-scale-dependent deformation mechanisms in incoherent metallic multilayered composites, Acta Mater 53 (18) (2005) 4817–4824.
- [11] A. Misra, M. Verdier, H. Kung, J.D. Embury, J.P. Hirth, Deformation mechanism maps for polycrystalline metallic multiplayers, Scripta Mater 41 (9) (1999) 973–979.
- [12] A. Misra, H. Kung, Deformation behavior of nanostructured metallic multilayers, Adv Eng Mater 3 (4) (2001) 217–222.
- [13] J.F. Archard, Contact and rubbing of flat surfaces, Journal of Applied Physics 24 (8) (1953) 981–988.
  [14] S. Izadi, H. Mraied, W.J. Cai, Tribological and mechanical behavior of nanos-
- tructured Al/Ti multilayers, Surf Coat Tech 275 (2015) 374–383.
- [15] W. Wang, R.N. Singh, Tribological behavior of Ni/Sn metallic multilayer composites, J Mater Eng Perform 7 (1) (1998) 27–32.
- [16] S.K. Ghosh, P.K. Limaye, B.P. Swain, N.L. Soni, R.G. Agrawal, R.O. Dusane, A.K. Grover, Tribological behaviour and residual stress of electrodeposited Ni/Cu multilayer films on stainless steel substrate, Surf Coat Tech 201 (8) (2007) 4609–4618.

[17] S.K. Ghosh, P.K. Limaye, S. Bhattacharya, N.L. Soni, A.K. Grover, Effect of Ni sublayer thickness on sliding wear characteristics of electrodeposited Ni/Cu multilayer coatings, Surf Coat Tech 201 (16-17) (2007) 7441–7448.

- [18] W. Cai, P. Bellon, Subsurface microstructure evolution and deformation mechanism of Ag-Cu eutectic alloy after dry sliding wear, Wear 303 (1-2) (2013) 602-610
- [19] Z.P. Luo, G.P. Zhang, R. Schwaiger, Microstructural vortex formation during cyclic sliding of Cu/Au multilayers, Scripta Mater 107 (2015) 67–70.
- [20] M. Linz, H. Winkelmann, K. Hradil, E. Badisch, F. Mucklich, Directional development of residual stress and surface fatigue during sliding contact, Eng Fail Anal 35 (2013) 678–685.
- [21] M. Rahsepar, M.E. Bahrololoom, Corrosion study of Ni/Zn compositionally modulated multilayer coatings using electrochemical impedance spectroscopy, Corros Sci 51 (11) (2009) 2537–2543.
- [22] J.Y. Fei, G.D. Wilcox, Electrodeposition of zinc-nickel compositionally modulated multilayer coatings and their corrosion behaviours, Surf Coat Tech 200 (11) (2006) 3533–3539.
- [23] S.R. Cross, R. Woollam, S. Shademan, C.A. Schuh, Computational design and optimization of multilayered and functionally graded corrosion coatings, Corros Sci 77 (2013) 297–307.
- [24] K.D. Ralston, N. Birbilis, M. Weyland, C.R. Hutchinson, The effect of precipitate size on the yield strength-pitting corrosion correlation in Al-Cu-Mg alloys, Acta Mater 58 (18) (2010) 5941–5948.
- [25] V.G. Shverina, V.K. Zaitsev, Standard Electrode-Potentials in Aqueous and Non-aqueous Solutions, Zh Fiz Khim 59 (7) (1985) 1696–1698 +.
- [26] D. Jones, Principles and Prevention of Corrosion, Prentice-Hall, Inc., New Jersey, USA, 1996.
- [27] W.C. Oliver, G.M. Pharr, AN IMPROVED TECHNIQUE FOR DETERMINING HARD-NESS AND ELASTIC-MODULUS USING LOAD AND DISPLACEMENT SENSING IN-DENTATION EXPERIMENTS, J. Mater. Res. 7 (6) (1992) 1564–1583.
- [28] R. Saha, W.D. Nix, Effects of the substrate on the determination of thin film mechanical properties by nanoindentation, Acta Mater 50 (1) (2002) 23–38.
- [29] D. Nelias, V. Boucly, M. Brunet, Elastic-plastic contact between rough surfaces: proposal for a wear or running-in model, Journal of Tribology-Transactions of the Asme 128 (2) (2006) 236–244.
- [30] K. Hokkirigawa, K. Kato, An experimental and theoretical investigation of ploughing, cutting and wedge formation during abrasive wear, Tribol Int 21 (1) (1988) 51–57.
- [31] E.M. Gutman, Mechanochemistry of solid surfaces, World Scientific Publishing Company1994.
- [32] L.Y. Xu, Y.F. Cheng, Development of a finite element model for simulation and prediction of mechanoelectrochemical effect of pipeline corrosion, Corros Sci 73 (2013) 150–160.
- [33] M. Hordon, B. Averbach, X-ray measurements of dislocation density in deformed copper and aluminum single crystals, Acta Metallurgica 9 (3) (1961)
- [34] G. Kresse, J. Furthmuller, Efficient iterative schemes for ab initio total-energy calculations using a plane-wave basis set, Physical Review B 54 (16) (1996) 11169–11186.
- [35] P.E. Blochl, Projector Augmented-Wave Method, Physical Review B 50 (24) (1994) 17953–17979.
- [36] G. Kresse, D. Joubert, From ultrasoft pseudopotentials to the projector augmented-wave method, Physical Review B 59 (3) (1999) 1758–1775.
- [37] J.P. Perdew, K. Burke, M. Ernzerhof, Generalized gradient approximation made simple, Phys Rev Lett 77 (18) (1996) 3865–3868.
- [38] C.V. Thompson, R. Carel, Texture Development in Polycrystalline Thin-Films, Mat Sci Eng B-Solid 32 (3) (1995) 211–219.
- [39] Y.F. Zhang, S. Xue, Q. Li, J. Li, J. Ding, T.J. Niu, R. Su, H. Wang, X. Zhang, Size dependent strengthening in high strength nanotwinned Al/Ti multilayers, Acta Mater 175 (2019) 466–476.
- [40] I. Kojima, B. Li, Structural characterization of thin films by X-ray reflectivity, Rigaku J 16 (2) (1999) 31.
- [41] J. Jensen, A. Oelkers, R. Toivola, D.C. Johnson, J. Elam, S. George, X-ray reflectivity characterization of ZnO/Al2O3 multilayers prepared by atomic layer deposition, Chemistry of materials 14 (5) (2002) 2276–2282.
- [42] J.Z. Hu, L. Chen, Effect of annealing on microstructure of Co/Cu multilayers, Journal of Materials Science-Materials in Electronics 26 (5) (2015) 3168– 3173.
- [43] V.G. Sathe, D. Phase, Interfacial reactions in Mo–Zr multilayer structure: an X-ray reflectivity study, Vacuum 77 (3) (2005) 301–306.
- [44] A. Misra, J. Hirth, R. Hoagland, Length-scale-dependent deformation mechanisms in incoherent metallic multilayered composites, Acta materialia 53 (18) (2005) 4817–4824.
- [45] B. Taljat, G.M. Pharr, Development of pile-up during spherical indentation of elastic-plastic solids, International journal of solids and structures 41 (14) (2004) 3891-3904.
- [46] J.Y. Zhang, J.J. Niu, X. Zhang, P. Zhang, G. Liu, G.J. Zhang, J. Sun, Tailoring nanostructured Cu/Cr multilayer films with enhanced hardness and tunable modulus, Materials Science and Engineering: A 543 (2012) 139–144.
   [47] K.Y. Yu, Y. Liu, S. Rios, H. Wang, X. Zhang, Strengthening mechanisms of
- [47] K.Y. Yu, Y. Liu, S. Rios, H. Wang, X. Zhang, Strengthening mechanisms of Ag/Ni immiscible multilayers with fcc/fcc interface, Surf Coat Tech 237 (2013) 269–275.
- [48] C. Kuphasuk, Y. Oshida, C.J. Andres, S.T. Hovijitra, M.T. Barco, D.T. Brown, Electrochemical corrosion of titanium and titanium-based alloys, The Journal of prosthetic dentistry 85 (2) (2001) 195–202.

- [49] F. Cao, G.-L. Song, A. Atrens, Corrosion and passivation of magnesium alloys, Corros Sci 111 (2016) 835-845.
- [50] A. Fateh, M. Aliofkhazraei, A. Rezvanian, Review of corrosive environments for copper and its corrosion inhibitors, Arabian journal of Chemistry (2017).
- [51] G.S. Wu, Fabrication of Al and Al/Ti coatings on magnesium alloy by sputtering, Mater Lett 61 (18) (2007) 3815–3817.
  [52] R.C. Zeng, K. Jiang, S.Q. Li, F. Zhang, H.Z. Cui, E.H. Han, Mechanical and corro-
- sion properties of Al/Ti film on magnesium alloy AZ31B, Front Mater Sci 9 (1) (2015) 66-76.
- [53] J. Chen, J. Xiao, J.D. Poplawsky, F.M. Michel, C. Deng, W. Cai, The origin of passivity in aluminum-manganese solid solutions, Corros Sci 173 (2020) 108749.
  [54] B. Zhang, Y. Li, F.J.C.s. Wang, Electrochemical corrosion behaviour of microcorporal line aluminimum in activities and the control of th
- crystalline aluminium in acidic solutions, Corrosion science 49 (5) (2007) 2071-2082.
- [55] Y.K. Zhu, J.D. Poplawsky, S.R. Li, R.R. Unocic, L.G. Bland, C.D. Taylor, J.S. Locke, E.A. Marquis, G.S. Frankel, Localized corrosion at nm-scale hardening precipitates in Al-Cu-Li alloys, Acta Mater 189 (2020) 204–213.
- [56] H. Yoshioka, Q. Yan, K. Asami, K. Hashimoto, Pitting Potential and Structure of Sputter-Deposited Al-Ti Alloys, Mat Sci Eng a-Struct 134 (1991) 1054–1057.
- [57] H. Mraied, W. Wang, W. Cai, Influence of chemical heterogeneity and microstructure on the corrosion resistance of biodegradable WE43 magnesium alloys, J Mater Chem B 7 (41) (2019) 6399-6411.
- [58] J. Zähr, S. Oswald, M. Türpe, H. Ullrich, U. Füssel, Characterisation of oxide and hydroxide layers on technical aluminum materials using XPS, Vacuum 86 (9) (2012) 1216–1219.
- M. Liu, Y. Jin, C. Leygraf, J.S. Pan, A DFT-Study of Cl Ingress into alpha-Al2O3(0001) and Al(111) and Its Possible Influence on Localized Corrosion of Al, J Electrochem Soc 166 (11) (2019) C3124-C3130.